

Monolayer PtSe₂, a New Semiconducting Transition-Metal-Dichalcogenide, Epitaxially Grown by Direct Selenization of Pt

Yeliang Wang,^{†,¶} Linfei Li,[†] Wei Yao,[‡] Shiru Song,[†] J. T. Sun,[†] Jinbo Pan,[†] Xiao Ren,[†] Chen Li,^{§,◆} Eiji Okunishi,[⊥] Yu-Qi Wang,[†] Eryin Wang,[‡] Yan Shao,[†] Y. Y. Zhang,^{||,§,†} Hai-tao Yang,[†] Eike F. Schwieter,[▽] Hideaki Iwasawa,[▽] Kenya Shimada,[▽] Masaki Taniguchi,[▽] Zhaohua Cheng,[†] Shuyun Zhou,^{*,‡,¶} Shixuan Du,^{*,†,¶} Stephen J. Pennycook,[○] Sokrates T. Pantelides,^{||,§} and Hong-Jun Gao^{*,†,¶}

[†]Beijing National Laboratory for Condensed Matter Physics, Institute of Physics, Chinese Academy of Sciences, Beijing 100190, China

[‡]State Key Laboratory of Low-Dimensional Quantum Physics and Department of Physics, Tsinghua University, Beijing 100084, China

[§]Materials Science and Technology Division, Oak Ridge National Laboratory, Oak Ridge, Tennessee 37831, United States

^{||}Department of Physics and Astronomy and Department of Electrical Engineering and Computer Science, Vanderbilt University, Nashville, Tennessee 37235, United States

[⊥]EM Business Unit, JEOL Ltd., Tokyo 196-8558, Japan

[¶]Collaborative Innovation Center of Quantum Matter, Beijing 100084, China

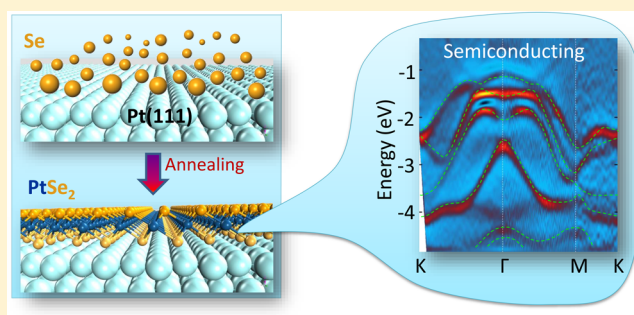
[▽]Hiroshima Synchrotron Radiation Center, Hiroshima University, Kagamiyama 2-313, Higashi-Hiroshima 739-0046, Japan

[○]Department of Materials Science and Engineering, National University of Singapore, Singapore 117576 Singapore

Supporting Information

ABSTRACT: Single-layer transition-metal dichalcogenides (TMDs) receive significant attention due to their intriguing physical properties for both fundamental research and potential applications in electronics, optoelectronics, spintronics, catalysis, and so on. Here, we demonstrate the epitaxial growth of high-quality single-crystal, monolayer platinum diselenide (PtSe₂), a new member of the layered TMDs family, by a single step of direct selenization of a Pt(111) substrate. A combination of atomic-resolution experimental characterizations and first-principle theoretic calculations reveals the atomic structure of the monolayer PtSe₂/Pt(111). Angle-resolved photoemission spectroscopy measurements confirm for the first time the semiconducting electronic structure of monolayer PtSe₂ (in contrast to its semimetallic bulk counterpart). The photocatalytic activity of monolayer PtSe₂ film is evaluated by a methylene-blue photodegradation experiment, demonstrating its practical application as a promising photocatalyst. Moreover, circular polarization calculations predict that monolayer PtSe₂ has also potential applications in valleytronics.

KEYWORDS: two-dimensional materials, transition-metal dichalcogenides, PtSe₂, epitaxial growth, monolayer, photocatalyst



Following the discovery of many unique properties of monolayer graphene and graphene analogues,^{1–5} attention has been paid to other two-dimensional crystalline materials with novel properties like sizable bandgap. Among them, layered TMDs with the general formula MX₂, where M represents a transition metal from groups 4–10 and X is a chalcogen (S, Se, or Te), are particularly desirable not only for fundamental research^{6–16} but also for technological development.^{17–22} Recent investigations of MX₂ have resulted in discoveries of dramatically different electronic structures at the monolayer limit compared to the bulk materials due to quantum confinement effects. For example, while pushing from bulk to monolayer, MoS₂ and MoSe₂ show an indirect-to-

direct bandgap transition.^{23–25} With these exciting findings, experimental research efforts so far have been mainly focused on semiconducting prototypical MX₂ with group VIB transition metals (M = Mo, W). In the large family of layered TMDs, many other promising single-layer TMDs and related quantum-defined properties remain to be explored experimentally. However, the synthesis and fabrication of high-quality,

Received: March 11, 2015

Revised: May 11, 2015

Published: May 21, 2015

monolayer TMDs materials other than group VIB ones remain a challenge.

In this Letter, we report epitaxial growth of monolayer PtSe_2 —a heretofore-unexplored member of the single-layer TMDs family—on a Pt substrate by direct “selenization”, an analog of direct oxidation. In contrast to conventional fabrication methods of MX_2 by exfoliation or chemical vapor deposition, the present route toward a monolayer dichalcogenide is very straightforward: only one element, Se, is deposited on a Pt substrate. The atomic structure of epitaxial PtSe_2 film has been determined by a combination of low-energy electron diffraction (LEED), scanning tunneling microscopy (STM), scanning transmission electron microscopy (STEM) measurements, and density functional theory (DFT) calculations. Angle-resolved photoemission spectroscopy (ARPES) measurements together with band structure calculations directly reveal monolayer PtSe_2 is a semiconductor, in contrast to a semimetal in its bulk form. In view of the simplicity of the production method and the advantages of the semiconducting nature, PtSe_2 film has potential for use in practical applications. Here, a photodegradation experiment based on as-prepared monolayer PtSe_2 film was performed, demonstrating its practical application as a visible light-driven photocatalyst. Moreover, circular polarization calculations indicate that monolayer PtSe_2 is a good candidate for valleytronics.

Monolayer PtSe_2 films were grown by a straightforward precursor-free method, that is, through a single step of direct selenization of a Pt(111) substrate (see schematic in Figure 1a).

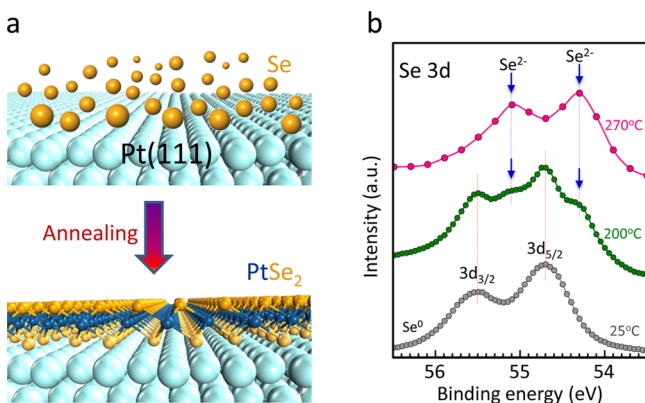


Figure 1. Growth process and XPS spectra of PtSe_2 film. (a) Schematic of the fabrication of PtSe_2 thin films by a single step of direct selenization of a Pt(111) substrate. PtSe_2 monolayer consists of one sublayer of Pt atoms sandwiched between two Se sublayers. The Pt spheres with different colors and sizes are used just to differentiate the Pt atoms in the Pt(111) substrate and in the PtSe_2 sublayer. (b) XPS measurements for the binding energies of Se during PtSe_2 growth demonstrating the formation of PtSe_2 at 270 °C. The blue arrows indicate the peak positions (55.19 and 54.39 eV) corresponding to the binding energy of Se^{2-} . The Se^0 peaks (at 55.68 and 54.80 eV) are dominant at 25 °C, whereas at 200 °C the peaks in the curve indicate the coexistence of Se^0 and Se^{2-} .

Selenium atoms were deposited on a Pt(111) substrate, and then the sample was annealed to ~ 200 °C to obtain epitaxial PtSe_2 films. The growth of PtSe_2 thin films was monitored by in situ X-ray photoemission spectroscopy (XPS). Figure 1b shows the XPS spectra of the Se 3d core level during PtSe_2 growth. When Se-deposited Pt(111) substrate is annealed to 200 °C, two new peaks appear at binding energies of 55.19 and 54.39 eV (labeled by the blue arrows), which can be explained by a

change in the chemical state of Se from Se^0 to Se^{2-} , corresponding to the selenization process of the sample. Further annealing of the sample to 270 °C results in the disappearance of Se^0 peaks (at 55.68 and 54.80 eV) and the dominance of Se^{2-} peaks, indicating full crystallization and complete formation of PtSe_2 films.

To obtain the structural information on the as-grown epitaxial films, the samples were characterized by LEED. Figure 2a shows a LEED pattern. Hexagonal diffraction spots from

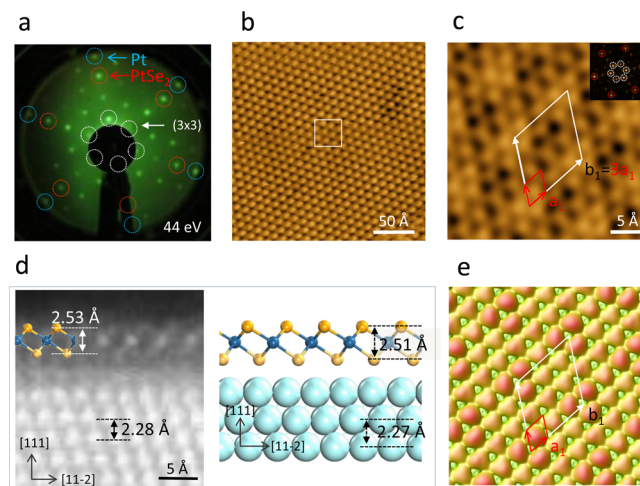


Figure 2. LEED pattern and atomic configuration of PtSe_2 film. (a) LEED pattern of a PtSe_2 film formed on the Pt(111) substrate. The blue, red, white circles indicate the diffraction spots from the Pt(111) lattice, PtSe_2 thin film and (3×3) superstructure with respect to PtSe_2 , respectively. (b) Large-scale STM image ($U = -1.9$ V and $I = 0.12$ nA) shows the moiré pattern of PtSe_2 thin film on Pt(111). The white rectangle marks the size of the close-up image in (c). (c) Atomic-resolution STM image ($U = -1.0$ V and $I = 0.12$ nA) of single-layer PtSe_2 showing the hexagonal lattice of Se atoms in the topmost sublayer of the PtSe_2 sandwich-type structure. A (3×3) moiré superstructure is visible. The red and white rhombi denote the unit cell of the PtSe_2 lattice and (3×3) superlattice, respectively. The inset displays the FFT pattern corresponding to PtSe_2 and the superstructure. (d) Side view of the atomic structure of the PtSe_2 monolayer on Pt(111). Left: atomic-resolution STEM Z-contrast image of the PtSe_2 /Pt(111) interface along the $[110]$ zone axis. A PtSe_2 single layer over the Pt(111) substrate is resolved at atomic scale with a model diagram overlaid for clarity. Right: the relaxed model. The blue and orange spheres represent Pt atoms and Se atoms, respectively. (e) Simulated STM image ($U = -1.0$ V) based on the calculated atomic structure in (d) is consistent with the experimental observation in (c).

PtSe_2 (red circles) are observed to have the same orientation as those from the Pt(111) substrate (blue circles), suggesting a rotational-domain-free growth. A (3×3) diffraction pattern of the epitaxial PtSe_2 film is clearly identified, which corresponds to a well-defined moiré superstructure arising from the lattice mismatch between the PtSe_2 film and Pt(111) substrate. Furthermore, identical LEED patterns were observed on the entire sample surface ($4 \text{ mm} \times 4 \text{ mm}$ in size), indicating the growth of a large-area, homogeneous and high-quality film.

To investigate the atomic structure of the PtSe_2 film, we performed STM studies. Figure 2b is a large-scale STM image with a well-ordered moiré pattern of PtSe_2 thin film on Pt(111). The periodicity of this moiré pattern is about 11.1 Å, four times the lattice constant of Pt(111). Figure 2c shows an atomic-resolution image of the area indicated by the white

square in Figure 2b, revealing hexagonally arranged protrusions with an average lattice constant of $a_1 = 3.7 \text{ \AA}$, which agrees perfectly with the interatomic spacing of Se atoms in the (0001) basal plane of bulk PtSe_2 . Therefore, we interpret the hexagonal protrusions in Figure 2c to be the Se atoms in the topmost Se plane of a PtSe_2 film. A regular (3×3) moiré superstructure with respect to the PtSe_2 lattice is then established, with a periodicity of $b_1 = 3a_1 \cong 11.1 \text{ \AA}$ (labeled by the white rhombus). The orientation of the moiré pattern is aligned with that of the PtSe_2 lattice. This is in agreement with the LEED observation (Figure 2a), where the diffraction spots of the (3×3) superlattice are in line with those of the PtSe_2 lattice. On the basis of LEED and STM measurements, the moiré pattern can be explained as the (3×3) PtSe_2 supercells located on the (4×4) $\text{Pt}(111)$ atoms (more discussion about the moiré pattern can be found in Figure S1 in the Supporting Information).

To gain further insight into interfacial features of the $\text{PtSe}_2/\text{Pt}(111)$ sample, we performed a cross-section high-angle annular-dark-field (HAADF) STEM study. A Z-contrast image of the $\text{PtSe}_2/\text{Pt}(111)$ interface is shown in Figure 2d. One bright layer combined with two dark layers observed on the topmost surface suggests a Se–Pt–Se sandwich configuration (as indicated by a model diagram superimposed in Figure 2d). The atomically resolved bulk Pt substrate lattice with an experimentally measured interlayer spacing of 2.28 \AA served as a reference for calibrating other spacing measurements. After the calibration, the spacing between the Se sublayers in the Se–Pt–Se sandwich is found to be 2.53 \AA , which is in agreement with the calculated value in single-layer PtSe_2 . These atomic-scale cross-section data obtained by STEM further verify that the fabricated structure is indeed a single-layer PtSe_2 film on the $\text{Pt}(111)$ substrate.

The combination of LEED, STM, and STEM studies indicates a (3×3) single-layer PtSe_2 on a (4×4) $\text{Pt}(111)$ structure. We then carried out DFT calculations based on this structure. The simulated STM image is shown in Figure 2e, in which the overall features of the experimental STM image (Figure 2c) are well reproduced. Only the hexagonally arranged Se atoms in the topmost sublayer of monolayer PtSe_2 are imaged. The remarkable agreement between the STM simulation and experimental STM observation strongly supports our conclusions and thus demonstrates the successful growth of a highly crystalline PtSe_2 monolayer.

Having grown highly crystalline single-layer PtSe_2 , we investigated its electronic energy band structure by ARPES. Figure 3a shows ARPES data measured along the high symmetry direction $\text{K}-\Gamma-\text{M}-\text{K}$ in the hexagonal Brillouin zone at a photon energy of 21.2 eV . Data taken at other photon energies show the same dispersion, confirming the 2D character of the monolayer PtSe_2 . Second-derivative spectra of raw experimental band structures (Figure 3a) are depicted in Figure 3b to enhance the visibility of the bands. Here, the top of the valence band is observed to be at -1.2 eV at the Γ point, and the conduction band is above the Fermi level, indicating that monolayer PtSe_2 is a semiconductor. It is quite different from the bulk PtSe_2 , which—according to calculations²⁶—is a semimetal. A direct comparison between the ARPES spectrum (Figure 3b) and the calculated band structure (green dotted lines in Figure 3b) shows excellent quantitative agreement. Combining the ARPES spectra with DFT calculations, we confirm that we have synthesized a single-layer PtSe_2 , and that the epitaxial PtSe_2 essentially has the same electronic properties

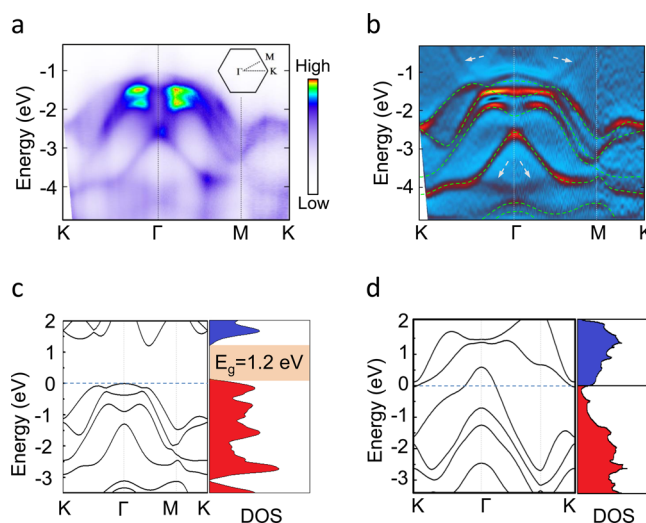


Figure 3. ARPES spectra and valence bands of single-layer PtSe_2 . (a) ARPES spectra obtained on the monolayer PtSe_2 on $\text{Pt}(111)$ along the $\text{K}-\Gamma-\text{M}-\text{K}$ directions in the hexagonal Brillouin zone (the high-symmetry directions are shown in the inset). (b) Second-derivative spectra of the raw ARPES data in (a). The calculated valence bands, superimposed as green dashed lines, are in excellent agreement with the experimental data. The bands marked by white arrows are from the Pt substrate. (ARPES result of clean $\text{Pt}(111)$ surface is shown in Figure S2 in Supporting Information.) (c), (d) Theoretically calculated band structure and density of states (DOS) of monolayer PtSe_2 and bulk PtSe_2 , respectively.

as the free-standing single-layer PtSe_2 . For the first time, the band structure of monolayer PtSe_2 films has been determined experimentally.

The semimetal-to-semiconductor transition was revealed by DFT-LDA calculations. As shown in Figure 3c, the band structure and density of state (DOS) suggest single-layer PtSe_2 is a semiconductor with an energy gap of 1.20 eV (2.10 eV bandgap is predicted from GW calculation²⁷). As a comparison, the band structure and DOS of bulk PtSe_2 are plotted in Figure 3d, which confirm that bulk PtSe_2 is semimetallic.²⁶ When increasing the thickness, bilayer PtSe_2 remains a semiconductor, but the energy gap decreases to 0.21 eV . Starting from a trilayer, PtSe_2 becomes semimetallic (calculated band structures of bilayer and trilayer PtSe_2 are listed in Figure S3 in the Supporting Information). Therefore, only single-layer PtSe_2 is a semiconductor with a sizable bandgap.

The opening of a sizable bandgap within the range of visible light makes monolayer PtSe_2 potentially suitable for optoelectronics and photocatalysis. We explored the photocatalytic properties of monolayer PtSe_2 by the degradation of methylene blue (MB) aqueous solution, which serves as a typical indicator of photocatalytic reactivity.^{28,29} The MB molecules adsorbed on the PtSe_2 films are degraded by electrons that are excited by visible light. The time-dependent degradation of MB with a single layer PtSe_2 catalyst was monitored by checking the decrease in the intensities of characteristic absorbance peaks of the MB molecules (shown in Figure 4). The photo degradation portion of MB molecules reached 38% after visible-light irradiation for 24 min. This rate is about four times faster than the rate obtained using PtSe_2 nanocrystals,³⁰ putting single-layer PtSe_2 in the same class as nitrogen-doped TiO_2 nanoparticles for photocatalysis.^{31,32}

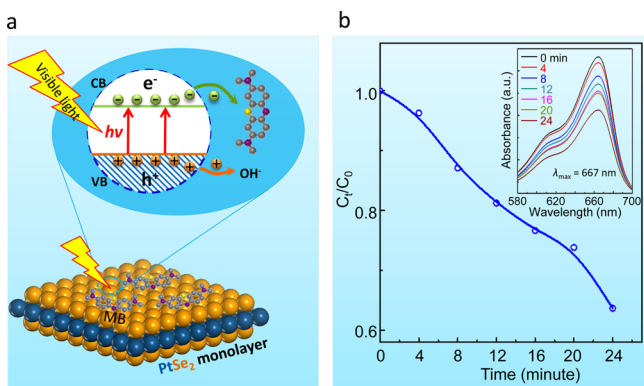


Figure 4. Photocatalytic activity of a single-layer PtSe₂ film. (a) Schematic diagram of the photocatalytic degradation of methylene blue (MB) molecules. Electrons and holes are excited by visible-light irradiation of epitaxial PtSe₂ monolayer films. The MB degradation by photoinduced electrons demonstrates the photocatalytic activity of PtSe₂ monolayer films. (b) Time trace of the normalized concentration (C_i/C_0 , where C_i and C_0 are the MB concentrations at time t min and 0 min, respectively) of the absorbance at a wavelength of 667 nm, the main absorbance peak of MB. The inset shows the UV-vis absorption spectra of MB, recorded at time intervals of 4 min.

With the existence of an energy gap in the single-layer PtSe₂, optical excitations can occur between the Γ point and the valley point along the Γ –M direction. This is reminiscent of the recently discovered valley-selective circular dichroism in MoS₂ by circularly polarized light.^{33–35} To explore this possibility, we calculated the degree of circular polarization of free-standing single-layer PtSe₂. The calculated circular polarization due to the direct interband transition between the top of the valence band (VB) to the bottom of the conduction band (CB) is shown in Figure 5a. It shows significant circular dichroism

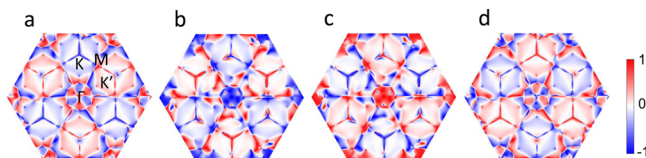


Figure 5. Momentum dependence of circular polarization of single-layer PtSe₂. (a–d) represent the calculated circular polarization due to the direct interband transition from the top of the valence band (VB1) to the bottom of the conduction band (CB1), from VB1 to the higher conduction band (CB2), from the lower valence band (VB2) to CB1, and from VB2 to CB2, respectively. Significant circular dichroism polarization exists along the M–K direction and near the Γ point.

polarization along the M–K direction and near the Γ point. In view of the indirect energy gap, this process can be assisted by lattice vibrations. It is noteworthy that the circular dichroism polarization not only exists in the transition between the top of the VB and the bottom of the CB, it also exists in transitions to higher energy levels. Circular dichroism polarization due to transitions from the vicinity of the VB to the vicinity of the CB can be clearly seen in Figure 5b, c, and d. Due to this significant circular polarization, in the presence of a nonvanishing in-plane electric field, the anomalous charge current driven by the Berry curvature would flow to the opposite edges, leading to a valley-polarized current and the resulting quantum valley Hall effect.^{36,37}

In summary, we have successfully fabricated high-quality, single-crystalline, monolayer PtSe₂ films, a new member of the TMDs family, through a single-step, direct selenization of a Pt(111) substrate at a relatively low temperature (~ 270 °C). Characterizations by LEED, STM, STEM, and DFT calculations elucidated both in-plane and vertical monolayer structures with atomic resolution. The ARPES measurements and their agreement with calculations revealed the semiconducting electronic structure of the single-layer PtSe₂. Together with the photocatalytic performance observed experimentally, monolayer PtSe₂ shows promise for potential applications in optoelectronics and photocatalysis. Moreover, the circular polarization of monolayer PtSe₂ in momentum space indicates a promising potential for valleytronic devices. Thus, our studies are a significant step forward in expanding the family of single-layer semiconducting TMDs and exploring the application potentials of thin TMDs in photoelectronic and energy-harvesting devices.

Methods. Sample Preparation. Single-layer PtSe₂ films were grown in an ultrahigh vacuum chamber, with a base pressure of 3×10^{-10} mbar, equipped with standard MBE capabilities. The Pt(111) substrate was cleaned by several cycles of Ar⁺ ion sputtering followed by annealing until sharp (1×1) diffraction spots in the LEED pattern and clean surface terraces in the STM images were obtained. High-purity Se evaporated from a Knudsen cell was deposited onto the clean Pt(111) surface at room temperature. The sample was subsequently annealed up to 270 °C to achieve selenization and crystallization. The growth process was monitored by XPS and LEED. After growth, the sample was transferred to an STM chamber for imaging and to an ARPES chamber for measuring the electronic band structure.

STEM Characterization. The cross-section image shown in Figure 2d was obtained from a JEOL JEM-ARM 200 operating at 200 kV with a sample prepared by a JEOL Ion Slicer. Practically identical images were also obtained from a Nion UltraSTEM 200 operating at 200 kV using a sample prepared with a Zeiss dual beam Focused Ion Beam instrument and a Fischione Nanomill. For the UltraSTEM 200, the probe-forming angle was ~ 30 mrad, and the inner angle of the HAADF detector was about 63 mrad. For the JEOL JEM-ARM 200, the probe-forming angle was 30 mrad, and the inner angle of the HAADF detector was about 90 mrad.

ARPES and XPS Measurements. The ARPES data were measured using both synchrotron radiation (BL-1 at HiSOR, Japan) and an ultraviolet lamp with He I α spectral line. For the synchrotron data the sample was held at 20 K. The energy analyzer was a VG Scienta 4000/8000 with total energy resolution set to less than 20 meV. The synchrotron XPS data were taken at a photon energy of 105 eV.

First-Principles Calculations. DFT calculations were performed within the local density approximation (LDA) by using the Vienna ab initio simulation package (VASP).³⁸ The projector augmented wave method was employed.³⁹ The periodic slab models included four layers of Pt substrate, one layer PtSe₂, and a vacuum layer of 15 Å. All atoms were fully relaxed except for the bottom two substrate layers until the net force on every atom was less than 0.01 eV/Å. The energy cutoff of the plane-wave basis sets was 400 eV, and the k-points sampling was $5 \times 5 \times 1$ with the Monkhorst–Pack scheme. The momentum dependence of the degree of circular dichroism of 1T-PtSe₂ is given by $\eta(k) = ((|P_+(k)|^2) - (|P_-(k)|^2)) / ((|P_+(k)|^2) + (|P_-(k)|^2))$, where $P_{\pm}(k) = P_a^c(k) \pm iP_a^v(k)$. The

direct interband optical transition matrix $P_{\alpha}^{ci}(k) = \langle u_{c,k} | \hat{p}_{\alpha} | u_{i,k} \rangle$ was obtained by DFT calculations, including spin-orbit coupling, where $u_{c,k}$ is the periodic part of the Bloch function. In the circular polarization calculations, the whole Brillouin zone was sampled with a very dense k -point grid of 14 400 points.⁴⁰

Photocatalytic Experiment. The photocatalytic activity of as-prepared monolayer PtSe₂ films was tested by catalytic degradation of methylene blue serving as a standard model dye under visible-light irradiation at room temperature. The ultraviolet/visible-light source was a 150 W Xe lamp located at a distance of 15 cm above the solution. A set of appropriate cutoff filters was applied to determine illumination wavelength and ensured that the photocatalytic reaction took place just under visible light. The as-prepared monolayer PtSe₂ films were exfoliated from the Pt(111) substrate by ultrasonication in aqueous solution. The Pt(111) crystal was picked out from the solution to avoid its possible influence on the photocatalytic activity. Then MB molecules and ethanol (0.01 mL) were added to the solution containing peeled PtSe₂ monolayers. Before photocatalytic reaction, the solution was kept in darkness for 1 h in order to achieve an adsorption-desorption equilibrium between the PtSe₂ film and MB molecules. After that, the suspension was exposed to visible-light irradiation. At time intervals of 4 min, solution samples were collected and their absorbance measured by a commercial ultraviolet-visible (UV-vis) spectrophotometer. Accordingly, the intensity changes of characteristic absorbance peaks of the MB molecules were recorded. The photocatalytic performance of PtSe₂ monolayers was thus evaluated by the time-dependent degradation rate C_t/C_0 shown in Figure 4b.

■ ASSOCIATED CONTENT

Supporting Information

Top view of the model of a PtSe₂ monolayer on a Pt(111), ARPES result of clean Pt(111), and calculated band structures of monolayer, bilayer, trilayer, and bulk PtSe₂. The Supporting Information is available free of charge on the ACS Publications website at DOI: 10.1021/acs.nanolett.5b00964.

■ AUTHOR INFORMATION

Corresponding Authors

*E-mail: hjgao@iphy.ac.cn.

*E-mail: sxdu@iphy.ac.cn.

*E-mail: syzhou@mail.tsinghua.edu.cn.

Present Address

◆Department of Lithospheric Research, University of Vienna, Vienna 1090, Austria.

Author Contributions

Y.W., L.L., W.Y., and S.S. contributed equally to this work. The manuscript was written through contributions of all authors.

Notes

The authors declare no competing financial interest.

■ ACKNOWLEDGMENTS

The authors thank Min Ouyang for constructive suggestions. We acknowledge financial support from the National Basic Research Program of China (Nos. 2013CBA01600 and 2011CB932700), National Natural Foundation of China (Nos. 61222112, 61390501, 51325204, 11334006, and 61306114), Chinese Academy of Sciences (Nos. 1731300500015 and XDB07030100) and the U.S. Department

of Energy grant DE-FG02-09ER46554 (STP). Supercomputer time was provided by the supercomputer center at Shanghai, the National Center for Supercomputing Applications, and the Extreme Science and Engineering Discovery Environment (XSEDE), which is supported by National Science Foundation grant ACI-1053575. The STEM work was supported by the U.S. Department of Energy, Office of Science, Basic Energy Science, Materials Sciences and Engineering Division and by the JEOL Company, Japan. The experiments at HiSor have been performed under the proposal No. 13-B-20 and 14-A-10. E.F.S. acknowledges support from the JSPS fellowship and the Alexander von Humboldt Foundation.

■ REFERENCES

- (1) Novoselov, K. S. *Rev. Mod. Phys.* **2011**, 83 (3), 837–849.
- (2) Novoselov, K. S.; Fal'ko, V. I.; Colombo, L.; Gellert, P. R.; Schwab, M. G.; Kim, K. *Nature* **2012**, 490 (7419), 192–200.
- (3) Meng, L.; Wang, Y.; Zhang, L.; Du, S.; Wu, R.; Li, L.; Zhang, Y.; Li, G.; Zhou, H.; Hofer, W. A.; Gao, H.-J. *Nano Lett.* **2013**, 13 (2), 685–690.
- (4) Li, L.; Wang, Y.; Xie, S.; Li, X.-B.; Wang, Y.-Q.; Wu, R.; Sun, H.; Zhang, S.; Gao, H.-J. *Nano Lett.* **2013**, 13 (10), 4671–4674.
- (5) Li, L.; Lu, S. z.; Pan, J.; Qin, Z.; Wang, Y. q.; Wang, Y.; Cao, G. y.; Du, S.; Gao, H. J. *Adv. Mater.* **2014**, 26 (28), 4820–4824.
- (6) Eda, G.; Yamaguchi, H.; Voiry, D.; Fujita, T.; Chen, M.; Chhowalla, M. *Nano Lett.* **2011**, 11 (12), 5111–5116.
- (7) Liu, K. K.; Zhang, W. J.; Lee, Y. H.; Lin, Y. C.; Chang, M. T.; Su, C.; Chang, C. S.; Li, H.; Shi, Y. M.; Zhang, H.; Lai, C. S.; Li, L. J. *Nano Lett.* **2012**, 12 (3), 1538–1544.
- (8) Lee, Y. H.; Yu, L. L.; Wang, H.; Fang, W. J.; Ling, X.; Shi, Y. M.; Lin, C. T.; Huang, J. K.; Chang, M. T.; Chang, C. S.; Dresselhaus, M.; Palacios, T.; Li, L. J.; Kong, J. *Nano Lett.* **2013**, 13 (4), 1852–1857.
- (9) Baugher, B. W. H.; Churchill, H. O. H.; Yang, Y. F.; Jarillo-Herrero, P. *Nano Lett.* **2013**, 13 (9), 4212–4216.
- (10) He, K.; Poole, C.; Mak, K. F.; Shan, J. *Nano Lett.* **2013**, 13 (6), 2931–2936.
- (11) Najmaei, S.; Liu, Z.; Zhou, W.; Zou, X.; Shi, G.; Lei, S.; Yakobson, B. I.; Idrobo, J.-C.; Ajayan, P. M.; Lou, J. *Nat. Mater.* **2013**, 12 (8), 754–759.
- (12) van der Zande, A. M.; Huang, P. Y.; Chenet, D. A.; Berkelbach, T. C.; You, Y.; Lee, G.-H.; Heinz, T. F.; Reichman, D. R.; Muller, D. A.; Hone, J. C. *Nat. Mater.* **2013**, 12 (6), 554–561.
- (13) Chhowalla, M.; Shin, H. S.; Eda, G.; Li, L.-J.; Loh, K. P.; Zhang, H. *Nat. Chem.* **2013**, 5 (4), 263–275.
- (14) Mai, C.; Barrette, A.; Yu, Y.; Semenov, Y. G.; Kim, K. W.; Cao, L.; Gundogdu, K. *Nano Lett.* **2014**, 14 (1), 202–206.
- (15) Fiori, G.; Bonaccorso, F.; Iannaccone, G.; Palacios, T.; Neumaier, D.; Seabaugh, A.; Banerjee, S. K.; Colombo, L. *Nat. Nanotechnol.* **2014**, 9, 768–779.
- (16) Elmaleh, E.; Saunders, A. E.; Costi, R.; Salant, A.; Banin, U. *Adv. Mater.* **2008**, 20 (22), 4312–4317.
- (17) Zhang, Y. J.; Ye, J. T.; Matsushashi, Y.; Iwasa, Y. *Nano Lett.* **2012**, 12 (3), 1136–1140.
- (18) Wang, H.; Yu, L. L.; Lee, Y. H.; Shi, Y. M.; Hsu, A.; Chin, M. L.; Li, L. J.; Dubey, M.; Kong, J.; Palacios, T. *Nano Lett.* **2012**, 12 (9), 4674–4680.
- (19) Wang, Q. H.; Kalantar-Zadeh, K.; Kis, A.; Coleman, J. N.; Strano, M. S. *Nat. Nanotechnol.* **2012**, 7 (11), 699–712.
- (20) Voiry, D.; Salehi, M.; Silva, R.; Fujita, T.; Chen, M. W.; Asefa, T.; Shenoy, V. B.; Eda, G.; Chhowalla, M. *Nano Lett.* **2013**, 13 (12), 6222–6227.
- (21) Koppens, F. H. L.; Mueller, T.; Avouris, Ph.; Ferrari, A. C.; Vitiello, M. S.; Polini, M. *Nat. Nanotechnol.* **2014**, 9, 780–793.
- (22) Eda, G.; Yamaguchi, H.; Voiry, D.; Fujita, T.; Chen, M. W.; Chhowalla, M. *Nano Lett.* **2011**, 11 (12), 5111–5116.
- (23) Splendiani, A.; Sun, L.; Zhang, Y.; Li, T.; Kim, J.; Chim, C.-Y.; Galli, G.; Wang, F. *Nano Lett.* **2010**, 10 (4), 1271–1275.

- (24) Tongay, S.; Zhou, J.; Ataca, C.; Lo, K.; Matthews, T. S.; Li, J.; Grossman, J. C.; Wu, J. *Nano Lett.* **2012**, *12* (11), 5576–5580.
- (25) Zhang, Y.; Chang, T.-R.; Zhou, B.; Cui, Y.-T.; Yan, H.; Liu, Z.; Schmitt, F.; Lee, J.; Moore, R.; Chen, Y.; Lin, H.; Jeng, H.-T.; Mo, S.-K.; Hussain, Z.; Bansil, A.; Shen, Z.-X. *Nat. Nanotechnol.* **2014**, *9* (2), 111–115.
- (26) Dai, D.; Koo, H. J.; Whangbo, M. H.; Soular, C.; Rocquefelte, X.; Jobic, S. *J. Solid State Chem.* **2003**, *173* (1), 114–121.
- (27) Zhuang, H. L.; Hennig, R. G. *J. Phys. Chem. C* **2013**, *117* (40), 20440–20445.
- (28) Houas, A.; Lachheb, H.; Ksibi, M.; Elaloui, E.; Guillard, C.; Herrmann, J. M. *Appl. Catal., B* **2001**, *31* (2), 145–157.
- (29) Gronvold, F.; Haraldsen, H.; Kjekshus, A. *Acta Chem. Scand.* **1960**, *14* (9), 1879–1893.
- (30) Wilson, J. A.; Yoffe, A. D. *Adv. Phys.* **1969**, *18* (73), 193.
- (31) Asahi, R.; Morikawa, T.; Ohwaki, T.; Aoki, K.; Taga, Y. *Science* **2001**, *293* (5528), 269–271.
- (32) Gole, J. L.; Stout, J. D.; Burda, C.; Lou, Y. B.; Chen, X. B. *J. Phys. Chem. B* **2004**, *108* (4), 1230–1240.
- (33) Cao, T.; Wang, G.; Han, W.; Ye, H.; Zhu, C.; Shi, J.; Niu, Q.; Tan, P.; Wang, E.; Liu, B.; Feng, J. *Nature Commun.* **2012**, *3*, 887.
- (34) Zeng, H.; Dai, J.; Yao, W.; Xiao, D.; Cui, X. *Nat. Nanotechnol.* **2012**, *7* (8), 490–493.
- (35) Mak, K. F.; He, K.; Shan, J.; Heinz, T. F. *Nat. Nanotechnol.* **2012**, *7* (8), 494–498.
- (36) Xiao, D.; Yao, W.; Niu, Q. *Phys. Rev. Lett.* **2007**, *99* (23), 236809.
- (37) Rycerz, A.; Tworzydło, J.; Beenakker, C. W. J. *Nat. Phys.* **2007**, *3* (3), 172–175.
- (38) Kresse, G.; Furthmüller, J. *Phys. Rev. B* **1996**, *54* (16), 11169–11186.
- (39) Blöchl, P. E. *Phys. Rev. B* **1994**, *50* (24), 17953–17979.
- (40) Adolph, B.; Furthmüller, J.; Bechstedt, F. *Phys. Rev. B* **2001**, *63* (12), 125108.